*Corresponding authors: farabi.bozheyev@gmail.com and mauricio.schieda@hereon.de

Influence of $SnWO_4$, SnW_3O_9, WO_3 phases in tin tungstate films on photoelectrochemical water oxidation

Farabi Bozheyev,[a-c]* Steffen Fengler,[a] Jiri Kollmann,[a] Daniel Abou-Ras,[d] Nico Scharnagl,[e] Mauricio Schieda[a]*

[a]Institute of Photoelectrochemistry, Helmholtz-Zentrum Hereon GmbH, Max-Planck-Str. 1, 21502 Geesthacht, Germany

[b]Institute of Applied Science and Information Technologies, Baizakov Str. 280, 050042 Almaty, Kazakhstan

[c]National Nanolaboratory, Al-Farabi Kazakh National University, al-Farabi Ave. 71, 050000 Almaty, Kazakhstan

[d]Department Structure and Dynamics of Energy Materials, Helmholtz-Zentrum Berlin für Materialien und Energie GmbH, 14109 Berlin, Germany

[e]Institute of Surface Science, Helmholtz-Zentrum Hereon GmbH, Max-Planck-Str. 1, 21502 Geesthacht, Germany

*Corresponding authors: farabi.bozheyev@gmail.com and mauricio.schieda@hereon.de

Key words: thin films, α-$SnWO_4$, SnW_3O_9, WO_3, crystallization, photocurrent density, transient surface photovoltage, photoelectrochemistry.

Abstract

An essential step towards enabling the production of renewable and cost-efficient fuels is an improved understanding the performance of energy conversion materials. In recent years, there has been a growing interest in ternary metal oxides. Particularly, α-$SnWO_4$ exhibited promising properties for application to photoelectrochemical (PEC) water splitting. However, the number of corresponding studies remains limited, and a deeper understanding of the physical and chemical processes in α-$SnWO_4$ is necessary. To this date, charge carrier generation, separation, and transfer have not been exhaustively studied for $SnWO_4$-based photoelectrodes. All these processes depend on the phase composition, not only α-$SnWO_4$, but also on the related phases SnW_3O_9 and WO_3, as well as on their spatial distributions resulting from the coating synthesis. In the present work, these processes in different phases of tin tungstate films were investigated by transient surface photovoltage (TSPV) spectroscopy, to complement the analysis of the applicability of α-$SnWO_4$ thin films for practical PEC oxygen evolution. Pure α-$SnWO_4$ films exhibit higher photoactivities than that of films containing secondary SnW_3O_9 and WO_3 phases, due to the higher recombination of charge carriers when these phases are present.

Introduction

Sustainable hydrogen fuel produced by photoelectrochemical (PEC) water splitting is a promising concept, which could be practically realizable if artificial leaf devices were efficient and stable over time.[1] In common PEC configuration, a photoelectrode is in direct contact with the electrolyte that generates hydrogen upon illumination. For instance, a record efficiency of 19 % was achieved by a GaInP/GaInAs/GaAs photoelectrode, a system prepared by complex methods and containing expensive and rare elements.[2] On the other hand, a system based on more abundant elements, $BiVO_4$-Fe_2O_3-2*p* c-Si (2*p* is series-connected two parallel c-Si solar cells), exhibited an efficiency of only 7.7%.[3] Another alternative is a direct photovoltaic-electrolysis that resulted in the highest efficiency of 30 % based on complex multi-junction GaInP/GaAs/GaInNAsSb/PEM with a light concentrator.[4] In the current state, still, these approaches are not sufficient for commercialization due to the imbalance between cost, efficiency and stability.[5]

*Corresponding authors: farabi.bozheyev@gmail.com and mauricio.schieda@hereon.de

Over the past five years, among the ternary metal oxides, n-type $SnWO_4$ was given increased attention owing to its optical properties (E_g ~ 1.7−2.0 eV), and its valence and conduction band edge positions suitable for water splitting. Maximum theoretical photocurrent densities of 14.5−22.5 mA cm^{-2}, corresponding to a solar-to-hydrogen (STH) efficiencies of 25−29 % can be expected according to the Shockley-Queisser (S-Q) limit.[6] However, there is only a limited number of publications including original reports and systematic reviews on α-$SnWO_4$ for solar energy applications.[7–25] In addition, only a handful of methods have been developed to synthesize this material. The main limiting factor for metal oxides is the small polaron hopping mechanism[26] and ionic point defects that lead to typically low charge-carrier mobilites of 10^{-3}– 10^{-1} cm^2 V^{-1} s^{-1}. In α-$SnWO_4$, furthermore, the carrier diffusion length (L_D~10−100 nm) is 10^3 times smaller than the penetration depth. These limitations may be overcome by nanostructuring and by improving the intrinsic crystalline quality, leading to enhanced charge-carrier transport.[23]

Various strategies have been explored in the past to improve the quality, efficiency, and stability of α-$SnWO_4$ for PEC water splitting. The orientation of the crystal planes is crucial for efficient water splitting. Naturally, different facets can be expected to have different defect densities and thus, would also exhibit different properties with respect to nonradiative recombination. Surface reconstructions of the different facets also play a role. A chaotic orientation of nanoplatelets on a conductive substrate has been shown to result in an increase of the recombination rate, while, an ordered orientation significantly reduced the influence of the recombination on the efficiency.[27] For instance, a higher proportion of active facets (100)- vs. (001)-planes has been reported to result in a 3-fold photocurrent density increase, up to 0.79 mA cm^{-2} at 1.23 V_{RHE}.[28] Hybrid density functional theory calculations suggest designing (110)- and (100)-oriented α-$SnWO_4$ would increase photoelectrocatalytic oxygen evolution reaction (OER) and hydrogen evolution reaction (HER).[16] The formation of oxygen vacancies in reductive atmosphere has been shown to lead to a significant improvement of the photocurrent.[9] In addition to improvement in the quality of bulk, chemical stability improvement is required on the surface. During the testing in an electrolyte, α-$SnWO_4$ tends to oxidize, i.e., to form SnO_2 on the surface, which acts as a hole-blocking layer. Different protection layers such as NiO_x and CoO_x were explored as well as operation at different electrolyte pH values.[7,17,19,27] However, none of these procedures has so far led to a stable performance, due to surface dissolution, showing there is still a need for suitable protection coatings.

In the present report, the focus is on understanding the influence of the phase composition of tin tungstate films (α-$SnWO_4$, SnW_3O_9, and WO_3) on photocurrent and charge carrier transfer by means of transient surface photovoltage (TSPV) and photoelectrochemical (PEC) characterization. The main finding is that the photocurrent depends on the composition of the phases in the tin tungstate films, which determine the kinetics of charge carrier generation and recombination.

Experimental methods

Preparation of films

n-Si, FTO, and quartz were used as substrates for the deposition of the $SnWO_4$ films. These substrates were cleaned with isopropanol for 10 min in ultrasound bath, rinsed with distilled water, dried in N_2 flow and then exposed to ozone for 10 min. Edges of the substrates were masked using Cu tape before the film deposition for the purpose of film-thickness measurements. For the synthesis of $SnWO_4$ films, first, W films were deposited by magnetron sputtering from a W target (99.95 %) using Ar gas (Fig. S1). The thicknesses of the films were controlled by a quartz crystal microbalance. Then, the W films were annealed at 500 °C in a muffle furnace over a period of 3 h in air to obtain tungsten trioxide (WO_3) films.

*Corresponding authors: farabi.bozheyev@gmail.com and mauricio.schieda@hereon.de

Subsequently, the WO_3 films were placed in an alumina boat within 1−2 cm of 0.5 g $SnCl_2$ powder (also placed in the boat), and the boat was covered with another boat of similar size (Fig. S2). The tube was pumped to about $2x10^{-2}$ mbar and then heated to achieve chemical reaction (Carbolite Gero 30−3000 °C)[17] at temperatures ranging from 350 to 650 °C during 1 h and cooled down afterwards. The resulting films were brownish in color in correspondence with the α-$SnWO_4$ phase.

Characterizations

Surface and structure. The surface morphology of the $SnWO_4$ films was studied by in an optical microscope (Keyence VK-X260 confocal laser scanning microscope (CLSM)). The structure and phase composition of $SnWO_4$ films were investigated using X-ray diffraction (XRD) in a Bruker D8 Discover X-Ray diffractometer. The morphology of $SnWO_4$ films was observed by scanning electron microscope (Zeiss EVO 15). The phonon modes of the $SnWO_4$ films were studied by Raman spectroscopy using a WITec alpha300 Raman Microscope with an excitation laser wavelength of 532 nm. EDX elemental distributions were acquired on polished cross-section specimens using a Zeiss UltraPlus scanning electron microscope equipped with an Oxford Instruments Ultim Extreme EDX detector. The beam energy and current were 7 kV and about 6 nA. The cross-section specimens were prepared each by gluing two sample stripes face-to-face together using epoxy glue, then polishing the cross-section surface mechanically and by using a focused Ar-ion beam.

Optical spectroscopy and ellipsometry. Transmittance spectra were obtained using an Agilent UV-vis Cary5000 spectrometer. Refractive indices (*n)* and extinction coefficients (*k)* were determined by spectroscopic ellipsometry by a J. A. Woollam RC2 ellipsometer. The spectra were measured at three different incident angles of 60, 65 and 70 degrees in a wavelength range between 210 and 2500 nm. Finally, the data were fitted with a Kramers–Kronig-consistent basis spline function.

TSPV measurements. Modulated transient surface photovoltage (TSPV) spectra were measured with 8 Hz (125 ms) modulated light in a fixed capacitor arrangement.[30] The energies for sample excitation were selected by a prism monochromator using the light of a 300W xenon lamp. An individual TSPV spectrum consists of a series of on-and-off experiments done at different light excitation energies. The sample was exposed to light and then remained in the dark during the first half and second half of 125 ms (8 Hz) long measurement period. The FTO-coated quartz electrode and the sample isolated from each other by mica served as the electrodes of the measurement capacitor. The signals of the measurements were recorded using an oscilloscope card (GaGe 1622 CompuScope).

X-ray photoelectron spectroscopy. XPS measurements were performed using a KRATOS AXIS Ultra DLD (Kratos Analytical, Manchester, United Kingdom) equipped with a monochromatic Al Kα anode working with 10mA @ 15 kV (150W). For the survey spectra a pass energy of 160 eV was used while for the region spectra the pass energy was 20 eV. The investigated area was 700 x 300 µm. For depth profiling, Ar etching was performed. The etching rate was about 6 nm min^{-1} related to Ta_2O_5 (acceleration voltage 3.8 kV with an extraction current of 100 µA). The evaluation and validation of the data were carried out with the software CASA-XPS version 2.3.25. Calibration of the spectra was done by adjusting the C1s signal to 284.5 eV. For quantification and deconvolution of the region files, background subtraction (Shirley or U 4 Tougaard) was performed before calculation.

*Corresponding authors: farabi.bozheyev@gmail.com and mauricio.schieda@hereon.de

Photoelectrochemical measurements. Current voltage (j-V), chronoampermetry, and open circuit voltage measurements were carried out with an Ametek VersaSTAT 4 Potentiostat. PEC testing was performed in a 3-electrode cell (Zahner PECC2) with a Pt ring counter electrode, an Ag/AgCl (3.5 M NaCl, $V^0_{Ag/AgCl}$= 0.209 V_{SHE}) was the reference electrode, and a prepared film on a Si or a FTO was the working electrode. The electrolyte was a sodium sulfate (0.5 M Na_2SO_4, pH = 7) solution. A strip of Cu tape was fixed on top of the FTO substrates before coating of the films to protect the bare contact. Afterwards, the Cu tape was removed, and fresh strip of adhesive Cu tape was connected to this bare contact for the PEC tests. The potential for j-V measurements was varied from -0.7 to 1.3 $V_{Ag/AgCl}$ with a 25 mV s^{-1} scan rate. A 300 W xenon lamp with an AM1.5G filter was used as a light source. For the chopped j-V measurements, a shutter between the lamp and the cell was opened and closed during 2 s periods. The voltage V_{RHE}, measured against the Ag/AgCl reference electrode, was converted into the reversible hydrogen electrode (RHE) scale using the Nernst equation: $V_{RHE} = V_{Ag/AgCl} + 0.0591 \times pH + V^o_{Ag/AgCl}$, where $V_{Ag/AgCl}$ is the applied potential, $V^o_{Ag/AgCl}$ is the standard potential of the Ag/AgCl reference electrode. The incident photon-to-current efficiency (IPCE) was measured by a Zahner CIMPS PEC workstation with a Zahner TLS03 tunable light source.

Results and discussion

Structural and morphological studies

A pristine tungsten film exhibits a cubic crystal structure with the (110) reflection at 40.13° as shown by X-ray diffraction (XRD) patterns (Fig. S3). The cubic structure of W films transforms into a monoclinic WO_3 phase (PDF 01-072-0677) after annealing at 500 °C in air. Detailed structural comparison of a WO_3 film with the standard diffraction pattern is shown in Fig. S3. This crystal structure was also identified in magnetron-sputtered WO_3 films.[31,32] Heating in vacuum of WO_3 films in the presence of $SnCl_2$ salt leads to their transformation into α-$SnWO_4$ films.[17] The initial thickness of a W film increases accordingly after oxidation and stannation depending on temperature due to the phase conversion followed by volume change (Fig. S3b). For instance, the thickness of 200 nm W film is increased to 290 nm WO_3 film (30 % at 500 °C), 450 nm $SnWO_4$ film (55 % at 500 °C), and 340 nm $SnWO_4$ film (41 % at 550 °C). A higher temperature of 550 °C tend to create conditions for fast in- and out- diffusion of $SnCl_2$ and WCl_6 vapors that do not allow for settling in the film compared to 500 °C. Therefore, the thickness of the film crystallized at higher temperature is less than for the film prepared at lower temperature. The Naturally, α-$SnWO_4$ exhibits an orthorhombic phase according to the standard diffraction pattern (PDF 01-070-1049). The Fig. 1a shows elementary crystal structure for an orthorhombic phase of α-$SnWO_4$. Detailed structural comparison of α-$SnWO_4$ film with the standard diffraction pattern is shown in Fig. S4.

To complement the XRD characterization, Raman spectra (Fig. 1b) were obtained, showing WO_3 signals with maximum peak positions at 718.7 cm^{-1} and 810.7 cm^{-1}, and α-$SnWO_4$ at 780 cm^{-1}. The XRD pattern and Raman spectra for α-$SnWO_4$ and WO_3 are similar to previous reports on detailed structural studies.[33] Optical properties of the $SnWO_4$ films were studied by spectroscopic ellipsometry. The absorption coefficient (α) and Tauc plot of α-$SnWO_4$ are compared with those of WO_3 (Fig. 1c). Similar to other well established materials (CIGS, CdTe, InP, perovskite, etc.),[34] α-$SnWO_4$ exhibits α over the whole shown spectral range ~10^5 cm^{-1} at 2.4 eV that is promising with respect to the potential charge carrier generation

*Corresponding authors: farabi.bozheyev@gmail.com and mauricio.schieda@hereon.de

due to the suitable band gap (E_g). The indirect bandgaps determined by the Tauc plots for α-$SnWO_4$ and WO_3 are 1.74 eV and 2.8 eV, which is consistent with literature reports.[8,11,35]

XRD patterns of the samples clearly show that full crystallization of α-$SnWO_4$ depends on the thickness of the WO_3 films and annealing temperatures (Fig. S5). The films thicker than 280 nm feature the WO_3 secondary phase, as indicated by a (002) reflection at 23.11° (Fig. S5a), while the films thinner than 160 nm are composed of only the α-$SnWO_4$ phase. This means that during crystallization at 450 °C, chosen as an optimal temperature by Zhu et al.,[17] Sn cannot diffuse through the whole film hindered by the thickness of WO_3 films. The discrepancy with that report may be attributed to differences in the experimental configuration affecting the crystallization conditions, for instance, the temperature calibration, tube diameter, powder positioning, boat geometry, etc. Therefore, variation of the temperature was done to study the crystallization of the α-$SnWO_4$ films in the furnace (Fig. 2). In this report, the optimum preparation condition was found to be 550-600 °C as shown below.

*Corresponding authors: farabi.bozheyev@gmail.com and mauricio.schieda@hereon.de

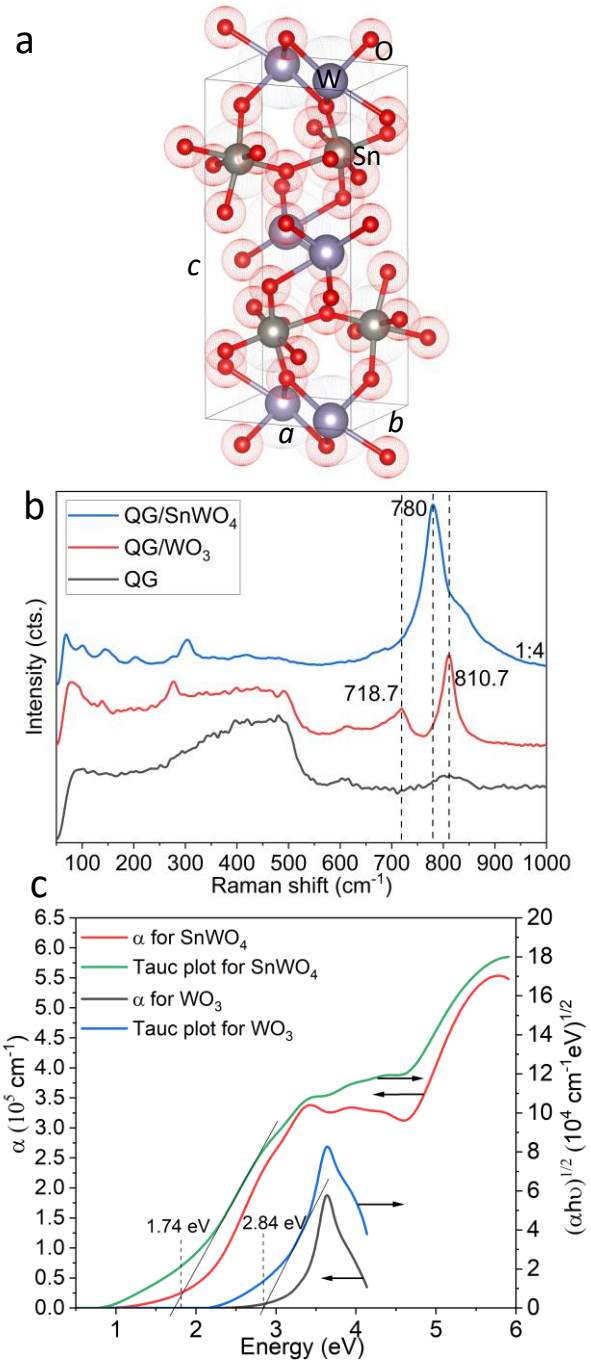


Figure 1. (a) Orthorhombic crystal structure of α-$SnWO_4$ crystallized at 450 °C. Gray, blue and red atoms represent W, Sn, and O. (b) Raman spectra of 110 nm thick WO_3 and 90 nm thick α-$SnWO_4$ films on n-Si substrates, their (c) absorption coefficient (α), and Tauc plots as a function of photon energy. The samples were prepared by oxidation of 50 nm thick W films at 500 °C and further stannation at 450 °C.

A series of WO_3 thin films were heated with $SnCl_2$ powder at different temperatures (Fig. 2). The WO_3 films gradually transform into $SnWO_4$ between 350 and 550 °C, depending on the thickness. An intensive reflection of a WO_3 phase at 23.05° (002) is still present for the thicker samples when the temperature is

*Corresponding authors: farabi.bozheyev@gmail.com and mauricio.schieda@hereon.de

increased up to 500 °C (Fig. S5b) and a slight reflection at 550 °C (Fig. S5c). At these temperatures, two phases coexist on thick films: WO_3 and $SnWO_4$. An indication of SnW_3O_9 phase can be already detected starting from 500 °C as a small reflection at 27.79° (002) for the thickest samples. This reflection significantly increases with further temperature rise to 650 °C (Fig. 2). At this temperature, complete transformation into SnW_3O_9 phase takes place (Fig. S6). The Raman spectra confirm the XRD results (Fig. S7), showing how different phase combinations are obtained with variation of temperature (Fig. 2). The thickest single phase 420 nm thick $SnWO_4$ film is achieved at 550 °C. Pure $SnWO_4$ films of 160 nm, 330 nm, and 350 nm are obtained at 450 °C, 500 °C, and 600 °C. A reaction furnace setup allowing further increase of the $SnCl_2$ concentration could lead to thicker $SnWO_4$ films, up to the micrometer range, however, that is out of the scope of the current work. EDX mapping of the film cross-sections reveals a homogeneous elemental distribution for films prepared at 500 °C and 550 °C (Fig. S8). Samples prepared at 600 °C are a composite of $SnWO_4$ and SnW_3O_9.

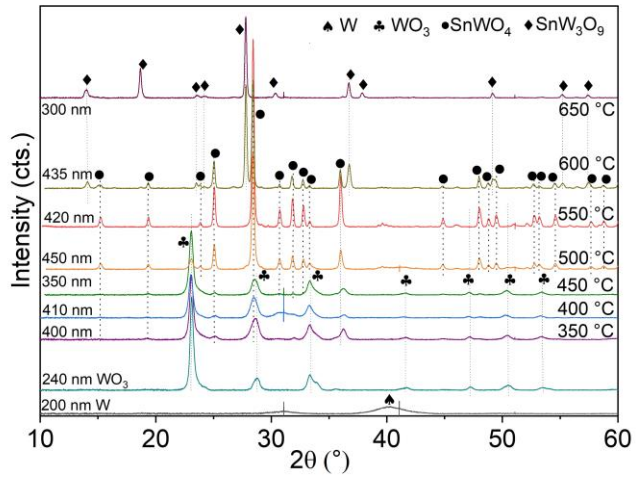


Figure 2. XRD patterns of the films prepared on n-Si substrates in the temperature range from 350 °C to 650 °C. See also the Raman spectra of the films in Fig. S9.

Further insight into the diffusion of Sn into WO_3 and the formation of $SnWO_4$ and SnW_3O_9 phases at different temperatures can be obtained from the SEM/EDX cross section mappings. The film synthesized at 500 °C consist of a $SnWO_4/WO_3/SnWO_4$ multilayer, i.e., pure crystallization of $SnWO_4$ is not possible (Fig. 3a). Sn diffuses easily into WO_3 from the top as well as from the bottom, since the ionic radii of Sn is 0.145 nm is significantly smaller than the lattice parameters of WO_3: a = 0.731 nm, b = 0.7603 nm, c = 0.7713 nm.[36] The reaction of formation of $SnWO_4$ can be written: $4WO_3 + 3SnCl_2 \rightarrow 3SnWO_4 + WCl_6\uparrow$. Voids and defects at the bottom of the film enhance the penetration of $SnCl_2$ vapor into the film as well as the diffusion of the byproduct WCl_6 out of the film. Thus, the reaction starts at the top and at the bottom of the film, which results in bands of higher Sn concentration towards the film surface and towards the Si substrate (a yellow line in Fig. 3a) on the EDX maps. In addition, the O poor region clearly indicates WO_3 (three O atoms to one W atom) compared to O reach region of $SnWO_4$ (four O atoms to one W atom). An intermediate WO_3 band can be clearly seen between the $SnWO_4$ bands. The full conversion into $SnWO_4$ is realized at 550 °C, where Sn, W, and O are homogeneously distributed across the film (Fig. 3b). Larger grains of $SnWO_4$ are formed, compared to those of the precursor WO_3, as evidenced by the narrower full width at half maximum (FWHM) of the most intensive peak for (121)-$SnWO_4$ with respect to (020)-WO_3 (Fig. 2). This would point to an increased mobility of Sn as a main factor leading to a full reaction with WO_3

*Corresponding authors: farabi.bozheyev@gmail.com and mauricio.schieda@hereon.de

at higher temperature. A possible mechanism for the Sn and W diffusion could then be similar to the interdiffusion of Cu and In in a $CuInS_2$ (CIS) film,[37] where Cu enrichment of Cu-poor CIS film leads to grain growth. This was similarly observed by decreasing FWHM of (112)-CIS peak during the recrystallization. Furthermore, as soon as Sn is incorporated in WO_3, there would be unequal diffusion of Sn and W through the vacancies according to Kirkendall effect.[38] This could be one reason for different crystallization mechanisms at 500 °C, 550 °C, and 600 °C in Fig. 3. The formation of $SnWO_4$ phase is expected at elevated temperatures. However, at 600 °C a secondary SnW_3O_9 phase is formed in addition to $SnWO_4$, on top of the film as well as towards the Si substrate (Fig. 3c, Fig. S10). Sn leaves the film bulk due to its higher mobility resulting in crystallization of a Sn poor phase: SnW_3O_9. This is clearly seen as highly concentrated W and O crystals oriented variously in space that indicate higher volatility of $SnCl_2$ compared to that of heavier WCl_6. A balance between in-diffusion of $SnCl_2$ and out-diffusion of WCl_6 in the films is achieved at 550 °C, favorable to the formation of α-$SnWO_4$. The EDX cross-section mappings of the films in high resolution for quantitative visualization are shown in Fig. S10. These results confirm the phase composition of $SnWO_4/WO_3$, $SnWO_4$, $SnW_3O_9/SnWO_4$ phases at 500 °C, 550 °C, and 600 °C, as revealed by the XRD data shown in Fig. 2.

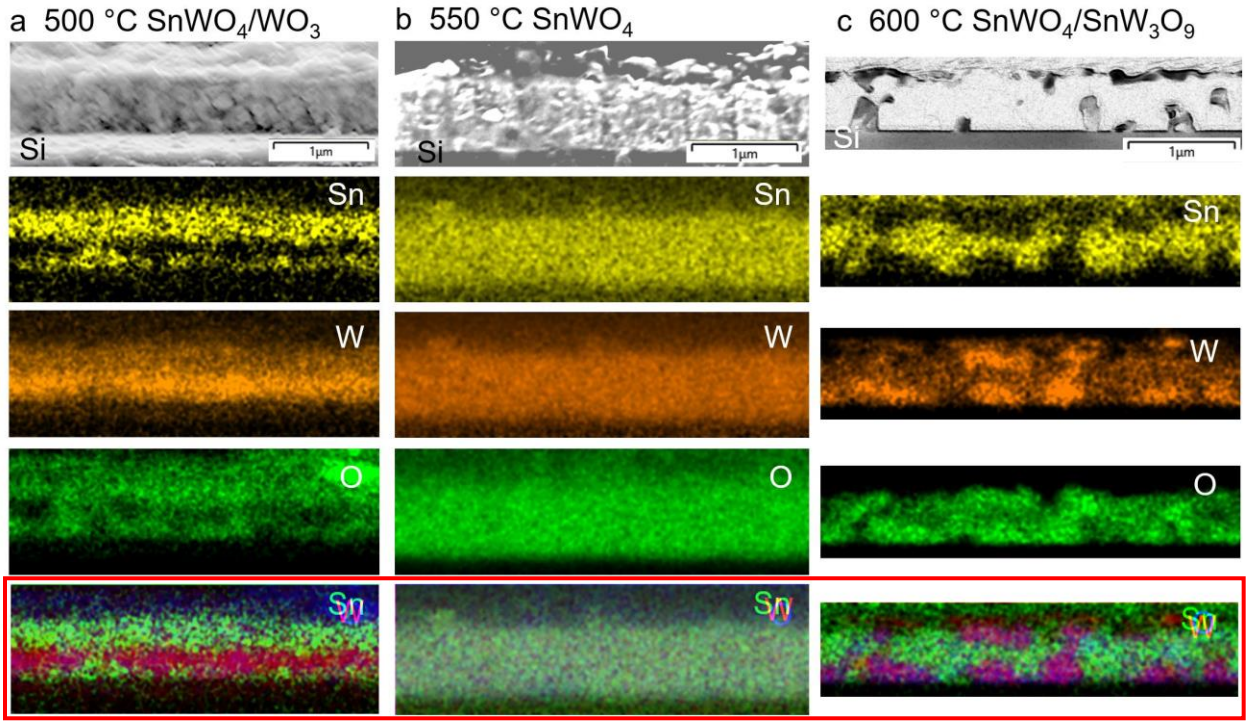


Figure 3. SEM and EDX images for (a) $SnWO_4/WO_3$, (b) $SnWO_4$, (c) $SnWO_4/SnW_3O_9$ films on n-Si prepared at 500 °C, 550 °C, and 600 °C. The colors of the elements: Sn-yellow, W-orange, O-green. Below in the red frame are the overlayed mappings: Sn-green, W- pink, O-violet.

The tin tungstate films prepared with various thicknesses at 600 °C exhibited $SnWO_4$ phase up to a thickness of about 350 nm (Fig. S5d). The film with the thickness of 435 nm shows presence of an additional hexagonal phase of SnW_3O_9 (PDF 01-086-0628).[39,40] Further increase in thickness led to the preferential formation of SnW_3O_9, as evidenced in the diffractograms for 540 nm, 590 nm and 640 nm thick films (Fig. S5d and Fig. S6). These results are confirmed by Raman spectra, where the Raman peak at 780 cm^{-1} disappears at higher film thickness (Fig. S7). This means that the rate and amount of a Sn diffusion

*Corresponding authors: farabi.bozheyev@gmail.com and mauricio.schieda@hereon.de

significantly influence on the crystallization of the films. Full crystallization of $SnWO_4$ for the thick films might be possible with higher amounts of $SnCl_2$ powder present. However, further addition of tin chloride powder and successive heating experiments at 600 °C did not result in transformation of SnW_3O_9 into $SnWO_4$ (Fig. S11). Therefore, the formation of SnW_3O_9 should be avoided if the objective is to get pure $SnWO_4$. SEM images of these films confirm the increase in crystallite size when the thickness increases from 90 nm to 350 nm (Fig. 4a,b). The transition into SnW_3O_9 is detected for a 435 nm thick film, where large platelets with white fine particles are seen on the surface (Fig. 4c). Bigger particles with crystalline SnW_3O_9 properties are confirmed by growing (200) reflection intensity and its decreasing full width at half maximum (Fig. S5d and Fig. 4c,d).

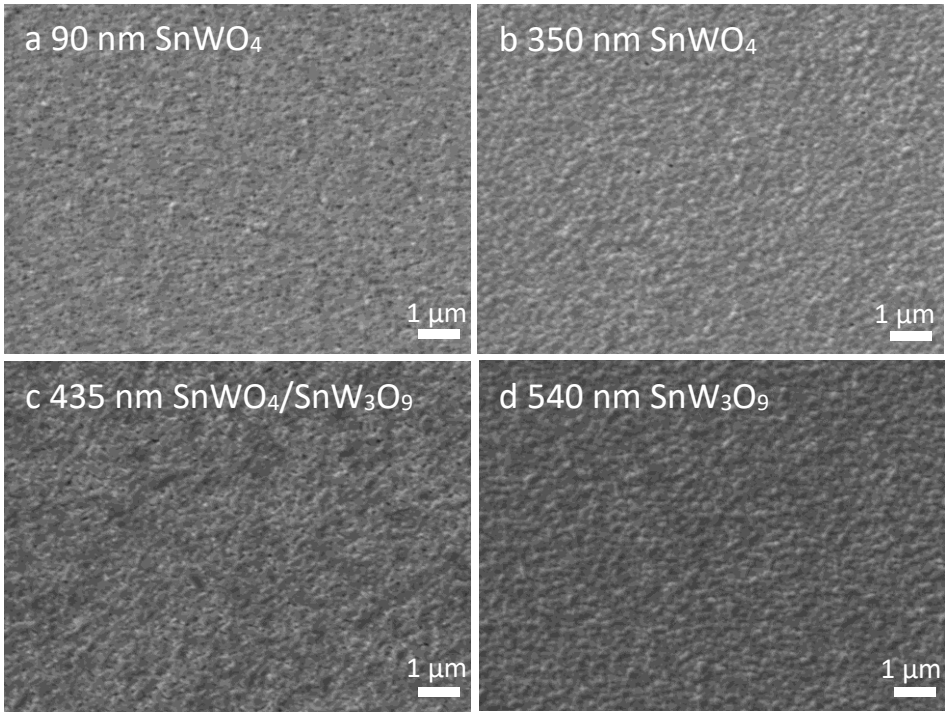


Figure 4. SEM images for (a) 90 nm $SnWO_4$, (b) 350 nm $SnWO_4$, (c) 435 nm $SnWO_4/SnW_3O_9$, and (d) 540 nm SnW_3O_9 films on n-Si prepared at 600 °C. SEM cross section images for $SnWO_4$ and SnW_3O_9 are shown in Fig. S12.

TSPV performance

TSPV measurements were performed on a series of tin tungstate phase samples with layer thicknesses between 90 and 630 nm prepared at CVD process temperatures of 500°C, 550°C, and 600°C and example spectra for each temperature are shown (Fig. 5a-c). All spectra show above the band gap a positive SPV-signal, indicating n-type behavior of the material. The maximum SPV amplitude (Fig. 5d) was found for all process temperatures between 300 and 450 nm indicating an optimum layer thickness for photoelectrodes of that material in the same range.

The individual transients that constitute the spectra were fitted in the light-on phase (t = 0...62.5 ms), each with a sum of 2 exponential functions. Each exponential function representing charge carrier transport processes with a characteristic time (τ_i). The fitting yielded for the 2 exponential functions amplitudes (A_i) and characteristic times as shown in Fig. 6a-c and 6d-f, respectively. The trends in the characteristic times and amplitudes look similar for all samples, except for the exponential function 2 of the 600°C sample. For

*Corresponding authors: farabi.bozheyev@gmail.com and mauricio.schieda@hereon.de

this sample an additional process at energies below 1.5 eV was found (that process was also described by the second exponential function). The amplitude of this additional process is shown in the insert of Fig. 6c. The low onset energy of that process around 0.5 eV is in good agreement with the band gap of SnW_3O_9. In the graphs showing the amplitudes, in addition also the DC-component of the SPV-signal was plotted. The DC-component describes the processes with a charge carrier dynamic that is too slow to follow the excitation frequency. For the 500°C and the 600°C samples, the DC-component followed a trend that is correlated with the amplitude spectra, while for the 550°C sample the DC-component was for energies below 2.7 eV unrelated to the excitation during the spectral measurement. In this range the signal was determined by discharging of the sample, while for energies above 2.7 eV the signal deviated abruptly from the prior discharging trend. This is constated exactly at the band gap of WO_3, indicating that the charge carrier transport dominating the DC-component is taking place in WO_3. The fact that already at the band gap the charging changes immediately points toward a high photon flux, indicating that the WO_3 layer in question is located at the surface where the exciting illumination wasn't already reduced by absorption in $SnWO_4$. The fact that the fluctuation in the DC-component also vanished after the onset of the absorption in WO_3 indicates that the whole signal of the DC-component originates at the surface and therefore that the discharging that takes place below 2.7 eV is a discharging of surface states at or nearby the WO_3 layer. For the 500°C/600°C sample the positive/negative DC-component that was correlated with the amplitude of process 1, indicates an accumulation of holes/electrons close to the surface.

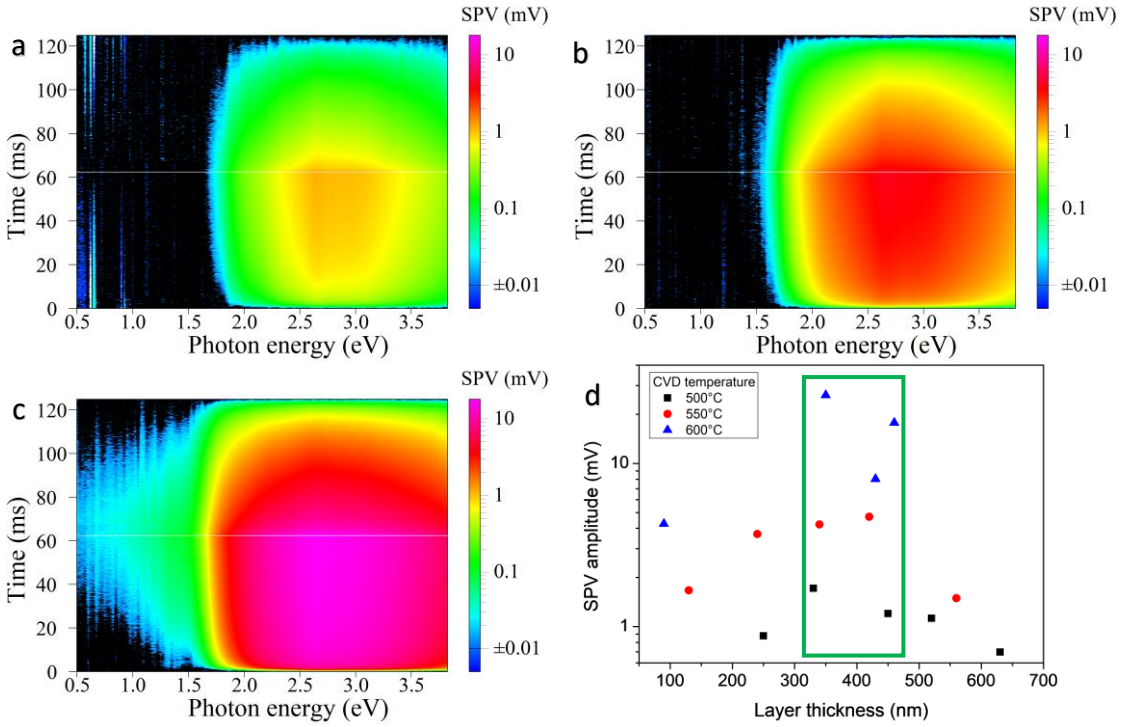


Figure 5. TSPV spectra of ~460 nm thick samples prepared at CVD temperatures of 500°C (a), 550°C (b) and 600°C (c) and maximum SPV-amplitude of TSPV spectra of samples of different layer thickness and prepared at different CVD process temperatures (d). The optimum film thickness region is shown with the green line to be the range of 300 – 450 nm.

In the small signals case, the SPV-signal can be assumed to be in good approximation linear dependent on the photon flux of the excitation. To get a better idea about the origin of the process that led to the

*Corresponding authors: farabi.bozheyev@gmail.com and mauricio.schieda@hereon.de

contributions of the SPV-signal described by the exponential functions, the amplitudes found by the fit were normalized against the photon flux, and the square root of the product of normalized SPV-amplitude and excitation energy was plotted (Fig. 6g-i). These plots are helpful to find the indirect transition energy related to the processes identified. For the 500°C sample transition energies of 1.74 and 1.59 eV were found for processes 1 and 2. The transition energy enabling the charge carrier transport process 1 is identical to the band gap found for $SnWO_4$ and can therefore be attributed to the band-band transition in $SnWO_4$. The transition energy of the first process was for all samples close to the band gap of $SnWO_4$ but decreasing in energy with increasing temperature. The transition energy of the second process was for all samples 170...180 meV below the first transition energy and decreased with increasing temperature. Also considering the n-type behavior of the samples, the most likely origin of that process is the transition between valance band and donor states.

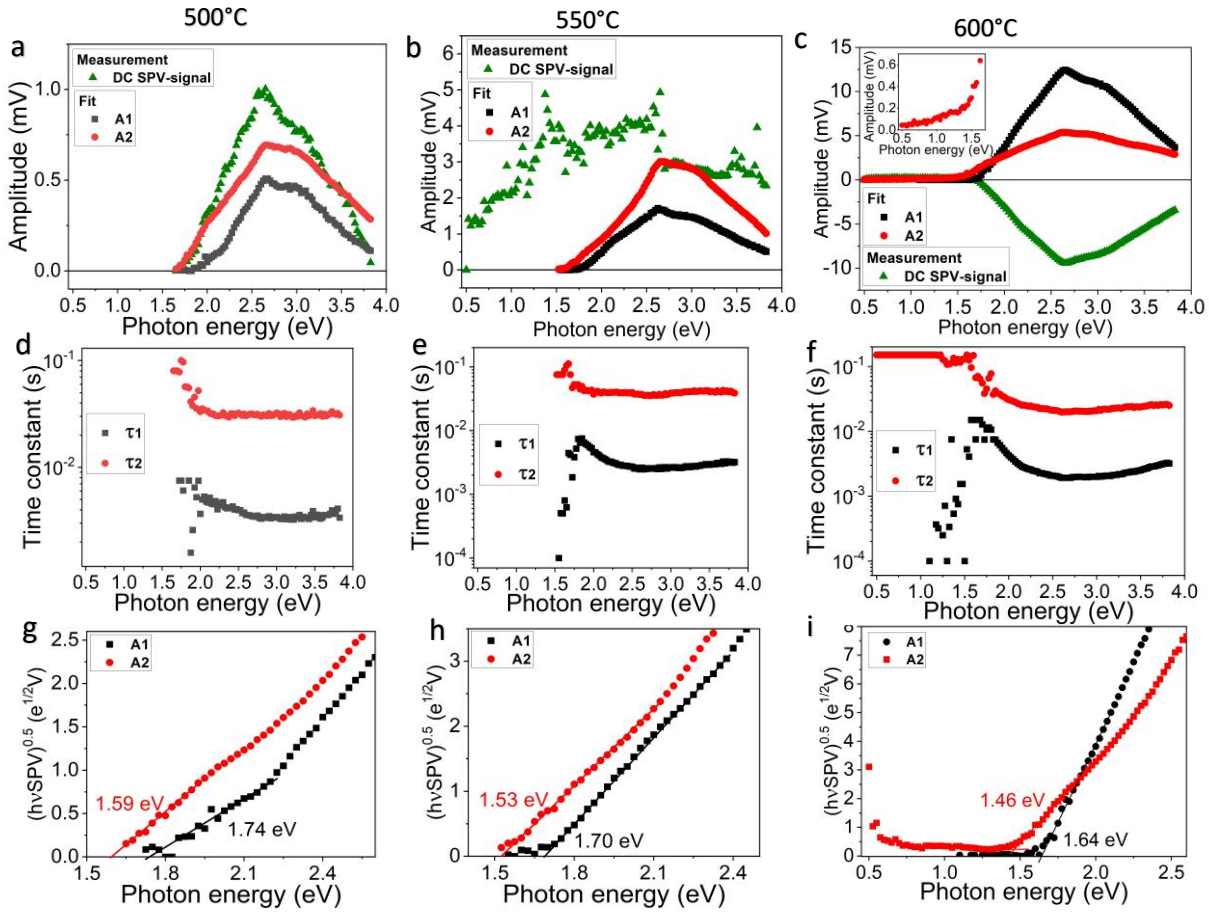


Figure 6. Amplitudes (a-c) and characteristic times (d-f) obtained by fitting of TSPV spectra of samples prepared at CVD temperatures of 500°C, 550°C and 600°C, as well as derived Tauc plots (g-i). Also shown are the DC-components of the SPV-signal (a-c).

The band schemes were derived from the analyzed SPV-measurements (Fig. 7). For the 500°C sample (Fig. 7a), an upwards band bending led to separation of holes towards the surface leading to a positive SPV-signal. The deep defects at the surface led to long trapping times for holes, resulting in a SPV DC-component with positive sign that followed the faster signal components (processes 1,2). There was no signature for the non-stoichiometric region in the $SnWO_4$-layer close to the substrate. For the 550°C sample (Fig. 7b), the DC-component was uncorrelated to the faster processes at lower excitation energy,

*Corresponding authors: farabi.bozheyev@gmail.com and mauricio.schieda@hereon.de

because the layer responsible for the signal was practically not accessible for charge carriers generated in the $SnWO_4$-layer. The DC-component only changed its character when charge carriers were photogenerated in the WO_3-surface layer. For the 600°C sample the slow processes that led to the negative DC-component was mainly due to electrons trapped in the near the surface SnW_3O_9 phases, after being photogenerated in a neighboring region without SnW_3O_9 surface layer and being separated over the $SnWO_4/SnW_3O_9$ heterojunction at the interface between those regions (see for comparison EDX cross sections of the 600°C sample in Fig. 3c). Therefore, the band scheme for the 600°C sample is in parts of the sample given by Fig. 7a, while it is in neighboring region given by a version of Fig. 7c with one or both shown SnW_3O_9-layers.

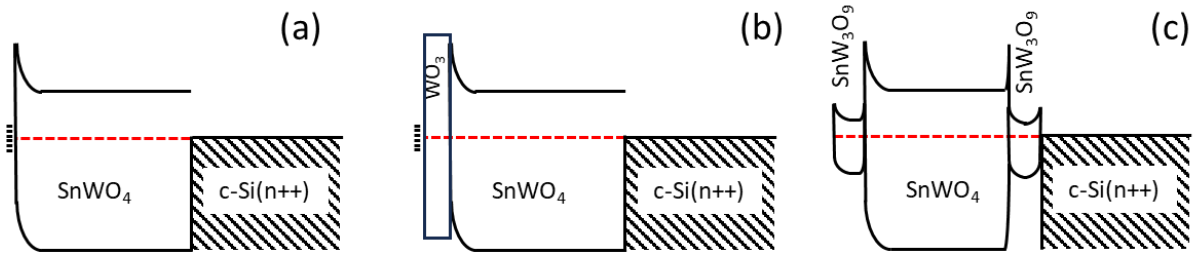


Figure 7. Band schemes derived from TSPV measurements for the 500°C (a) and the 550°C (b) sample. For the 600°C sample (a) and (c) need to be considered.

XPS studies

The X-ray photoelectron spectroscopy (XPS) spectra for samples of different thickness prepared at 600 °C were obtained at increasing etch depths, to investigate the elemental distribution in the films (Fig. 8). All films contain carbon on the surface, as is clear from the higher concentrations in the beginning of the etching process. This carbon contamination comes from the environment e.g., plastic substrate holder, the rest in the muffle oven that can be deposited during crystallization, etc. After removal of the surface carbon, a clear one-to-one relation between Sn and W is evidenced, which confirms crystallization of the 350 nm thick $SnWO_4$ film (Fig. 8a). Increasing thickness up to 435 nm results in about 3 times higher W concentration compared to Sn concentration (~10 to ~30 at. %), indicating formation of the mixture $SnWO_4/SnW_3O_9$ (Fig. 8b). At higher thickness up to 540 nm, about 4 times higher W concentration with respect to Sn (~10 to ~40 at. %) is evidenced, due to the formation of SnW_3O_9 (Fig. 8c). The concentration of O remains almost constant over the thickness for all films (~45 to ~55 at. %). The last etching phase shows a maximum Si composition of about 60-70 at. %, as the substrate is increasingly probed, due the removal of the Sn, W, and O. The [Sn]/[W] ratio shows quantitatively (Fig. S5d) the evolution of phase composition from $SnWO_4$, $SnWO_4/SnW_3O_9$, and SnW_3O_9 phases during the etch process, from the surface and into the bulk of the film (Fig. 8d). The [Sn]/[W] ratio for the 350 thick film is close to 1 corresponding to pure $SnWO_4$. For the 435 thick film the ratio is about 0.4, due to the presence of a mixture of $SnWO_4/SnW_3O_9$. For the 540 thick film, the ratio is close to 0.25, corresponding to SnW_3O_9.

*Corresponding authors: farabi.bozheyev@gmail.com and mauricio.schieda@hereon.de

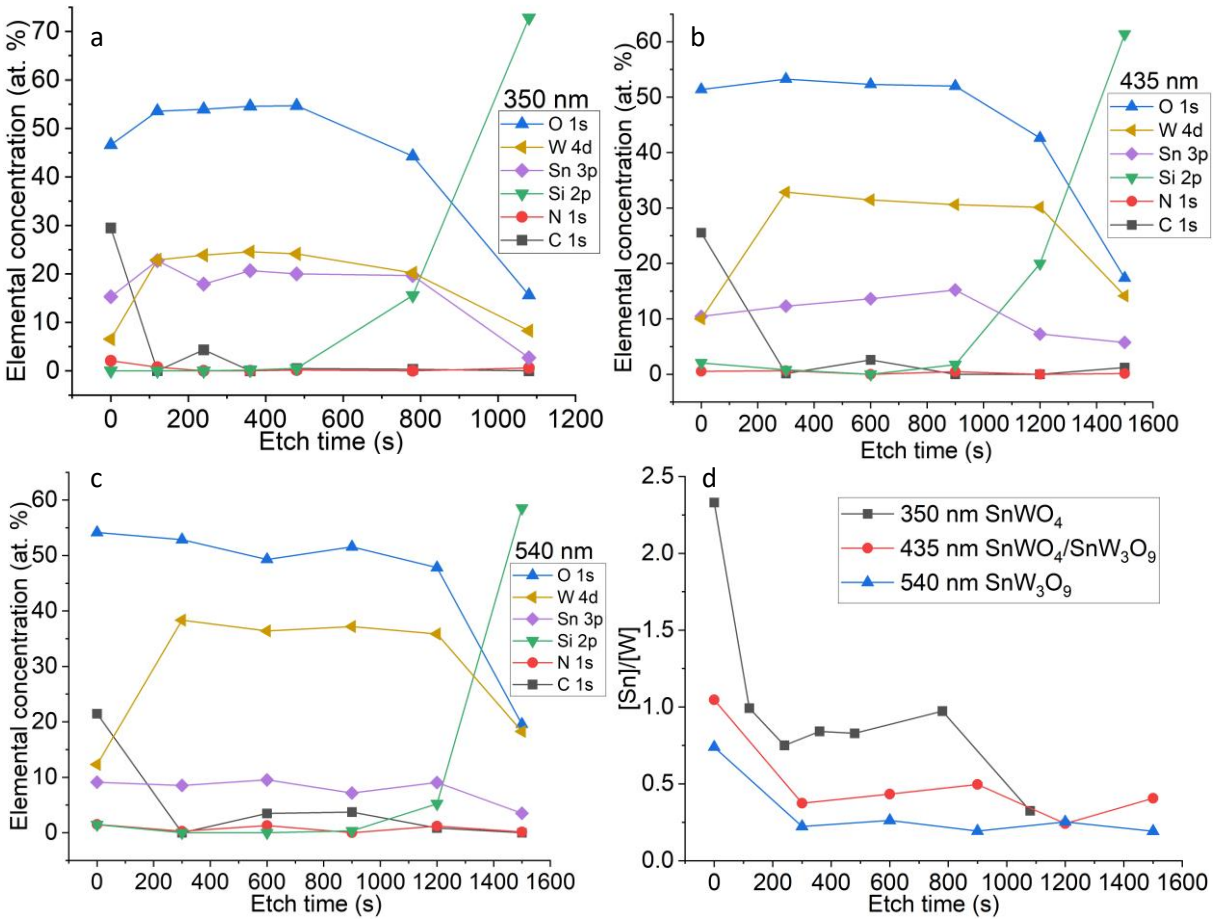


Figure 8. XPS spectra evolution of (a) 350 nm thick $SnWO_4$, (b) 435 nm thick $SnWO_4/SnW_3O_9$, and (c) 540 nm thick SnW_3O_9 films crystallized at 600 °C as a function of etch time. (d) [Sn]/[W] ratio as a function of etch time.

PEC performance

An increase in the $SnWO_4$ film thickness from 90 nm to 350 nm results in a clear improvement of the photocurrent density *j* (Fig. 9a-d). The 350 nm film showed the best photocurrent densities. The mixture $SnWO_4/SnW_3O_9$ showed a decrease in the photocurrent response, due to the contribution of SnW_3O_9. The main reason for *j* decrease is a junction formation between $SnWO_4/SnW_3O_9$ and low minority carrier diffusion length L_D of the charge carriers, resulting in limited lifetime within the thicker film.[7] All films on Si exhibit *j* in the range of 1−15 μA cm^{-2}, significantly lower than the films prepared on FTO. The OCP measurements agree with the photocurrent results. The 90 nm $SnWO_4$, 350 nm $SnWO_4$, 435 nm $SnWO_4/SnW_3O_9$ and 540 nm SnW_3O_9 thick films on n-Si resulted in V_{OC} values of 0.10, 0.14, 0.07, and 0.05 V (Fig. 9e). The highest dark current is observed for the SnW_3O_9 film, and the lowest for $SnWO_4$ that indicates the lowest resistivity for SnW_3O_9 and highest resistivity for $SnWO_4$ (Fig. S13). The mixture of $SnWO_4/SnW_3O_9$ exhibited an intermediate dark current. This observation proves that $SnWO_4$ and SnW_3O_9 are not formed as separate layered films, intermixing instead through the film's bulk. In case of a layered film formation, the resistivity of $SnWO_4$ would remain at least as high as that observed for the thinnest 90 nm $SnWO_4$ film.

*Corresponding authors: farabi.bozheyev@gmail.com and mauricio.schieda@hereon.de

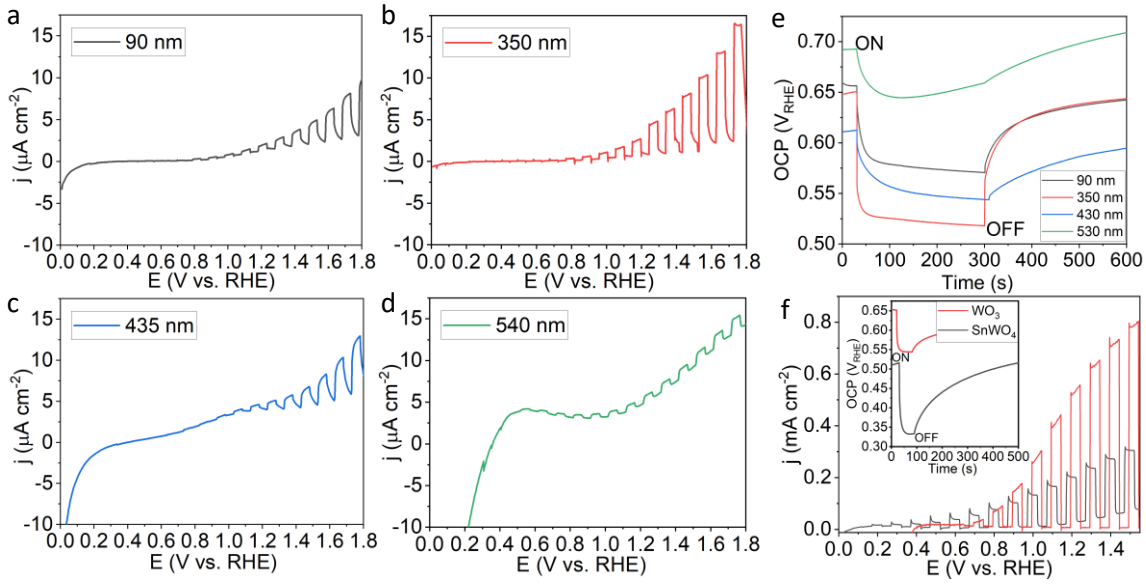


Figure 9. Linear scan voltammetry for (a) 90 nm $SnWO_4$, (b) 350 nm $SnWO_4$, (c) 435 nm $SnWO_4/SnW_3O_9$ and (d) 540 nm SnW_3O_9 thick films on n-Si in 0.5 M Na_2SO_4 and (e) their OCP. (f) Comparison of the linear scan voltammetry for a 400 nm WO_3 film prepared at 500 °C in air and transformed into a 520 nm $SnWO_4$ film at 450 °C with $SnCl_2$ powder in vacuum on FTO substrates in 0.5 M Na_2SO_4.

The PEC performances for WO_3 and $SnWO_4$ films are compared in Fig. 9f. The WO_3 film shows higher photocurrent density at positive potentials. The photocurrent densities *j*, measured at 1.21 V_{RHE}, were 0.17 and 0.53 mA cm^{-2} for $SnWO_4$ and WO_3 respectively. However, the $SnWO_4$ film shows *j* response starting at 0.07 V_{RHE}, and at 0.60 V_{RHE} for WO_3. Lower onset potential is an indication for lower energy needed to drive the photoelectrochemical reaction. As discussed, $SnWO_4$ has a more suitable conduction and valence band positions, that straddle both HER and OER potentials.[8] With the increasing potential, the dark current for $SnWO_4$ increases, compared to WO_3 (Fig. 9f). This has been attributed to the formation of SnO_2 and WO_3.[35] Further cycling leads to a decrease of *j* and dark current due to self-passivation, as SnO_2 serves as a hole-blocking layer (Fig. S14). Stabilization efforts in different pH values and with the NiO_x protection coating have been reported in the literature.[8,21] It was found that $SnWO_4$ does not degrade in acidic up to neutral conditions at pH values of 2, 5, 7 but in alkaline solution starts to decompose at pH 9 and 13 upon illumination. Furthermore, 24 h of testing led to the dissolution of NiO_x in the electrolyte. In this work, in an attempt to stabilize $SnWO_4$, an overlayer of 20 nm TiO_2 was deposited by atomic layer deposition (ALD). PEC testing showed a significant *j* decrease, and still oxidation of $SnWO_4$ (Fig. S15 and S16). The chrono-amperometry curve shows a positive dark current in the beginning, which decreases over time. Other possible protection coatings should be explored to protect the surface of $SnWO_4$ without reducing its activity.

Interestingly, the measured V_{OC} = 0.185 V for $SnWO_4$ is higher than V_{OC} = 0.110 V measured for WO_3, in inverse relationship to the measured photocurrents. For the wider E_g ($SnWO_4$: 1.74 eV and WO_3: 2.8 eV, Fig. 1d) higher V_{OC} is expected. This may be explained by better charge carrier separation in the film bulk for $SnWO_4$, accompanied, however, by weaker charge transfer from the film across the semiconductor/electrolyte junction. Smoother surface (smaller surface area) for WO_3 on FTO can be also a factor that contributes reducing the photon flux at the surface and producing a lower photovoltage. This

*Corresponding authors: farabi.bozheyev@gmail.com and mauricio.schieda@hereon.de

observation is clear from the transmittance spectra for WO_3 that shows interference fringes due to the more surface homogeneity (Fig. S17).

The PEC performance of $SnWO_4$ was studied on top of different substrates. It has been found that *j* is significantly lower on Si than on TiN:O and FTO (Figs. 9 and S18). The morphology of the films is rougher and therefore *j* is higher due to the higher surface area in these substrates (Figs. S19 and S20). LSV curves for $SnWO_4$ films show that the films are not stable after cycling compared to more stable WO_3 on FTO substrates (Figs. S21 and S22). Furthermore, crystallization depends on type of the substrate. Dendrite structure was organized on quartz glass substrate for a 100 nm thick $SnWO_4$ film at 450 °C (Fig. S23). Such kind of oak tree leaf structures are crystallized as a result of attachment of Sn, W, and O atoms to the nucleation centers (particles) or inhomogeneities. The film prepared at 600 °C exhibits the weak adhesion to the substrate and therefore agglomerates on the surface as spate particles (Fig. S24). The homogeneous $SnWO_4$ surface tends to grow only on Si compared to quartz, FTO, and TiN:O.

The measured j = 0.17 mA cm^{-2} is 100 times lower than the theoretical maximum $j \sim 17$ mA cm^{-2} under AM1.5G solar irradiation, expected for E_g = 1.9 eV and considering that 100 % of photons are absorbed by $SnWO_4$. There have been no reports demonstrating photocurrents beyond 2.0 mA cm^{-2}, the maximum experimentally measured *j* being 1.05 mA cm^{-2} at 0 V_{RHE} for $SnWO_4$.[41] This clearly indicates that the quality of the films should be significantly improved. Temperatures higher than 450 °C led to the inhomogeneous crystallization (phase-separation, agglomeration) of the films on FTO substrates due to the higher mobility of Sn and different expansion coefficients of WO_3 and FTO. Therefore, possible strategies for the improvement of coating adhesion should be further investigated.

A comprehensive review on the $SnWO_4$ for PEC water oxidation has been reported recently.[34] Different scavengers were used to boost the charge carrier transport from the semiconductor into electrolyte to investigate the maximum performance. The summary from all current reports is that the main efforts should be directed to elaboration of protection coatings that could stabilize the surface of $SnWO_4$ against SnO_2 formation and in turn boost *j*. Furthermore, the generated photovoltage V_{OC} = 0.185 V is very low to drive water splitting (1.23 V), even though in theory E_g = 1.74 eV of $SnWO_4$ should be close to optimum. Herein, the main losses are attributed to the series resistances, adhesion, defects, low $L_D \sim 75$ nm[23] and recombination in the bulk, and at the semiconductor-electrolyte interface. To achieve the maximum theoretical j = 17 mA cm^{-2}, a film thickness of about 10 µm would be necessary.[23] This thickness is significantly larger than the minority carrier diffusion length L_D, which is a main limiting factor considering expected losses at grain boundaries and defects in the structure. This issue remains the main challenge for many ternary metal oxides. Each factor should be further investigated for these materials.[12,42] Generally, stabilization of any photoelectrode surfaces for PEC water splitting is an open question that hinders their wide scale implementation in practice. The main requirement is that the protection coating should be electrochemically stable, while not hindering *j*, V_{OC}, and light absorption, and should be cost effective. Even though $SnWO_4$ exhibits a high absorption coefficient $\alpha \sim 10^5$ cm^{-1} (Fig. 1c) and the promising E_g value, allowing absorption of the most visible part of the solar spectra, and optimum valence and conduction band positions for the redox reaction of water, the carrier dynamics of the films should be further improved.

Conclusion

The influence of the temperature and W thickness on the crystallization of tin tungstate films was investigated. A series of WO_3 thin films were converted into $SnWO_4$ by reaction with $SnCl_2$ at increasing

*Corresponding authors: farabi.bozheyev@gmail.com and mauricio.schieda@hereon.de

temperatures. The synthesis of $SnWO_4$ and SnW_3O_9 can be controlled by the temperature and the thickness of the WO_3 films. High temperatures (500–650 °C) and thicknesses higher than 435 nm led to the formation of SnW_3O_9 phase, while lower thicknesses resulted in single-phase $SnWO_4$ films. At lower temperatures (T<450 °C) films of thickness beyond 280 nm still exhibit WO_3 phase along with $SnWO_4$. However, thinner films crystallize preferentially as $SnWO_4$. The presence of SnW_3O_9 phase in the films leads to reduced device performance, i.e. its formation needs to be impeded by controlling temperature and thickness of the films. The optimal temperatures and thicknesses for the preparation of single-phase $SnWO_4$ films with the best transient surface photovoltage (TSPV) and photoelectrochemical cell (PEC) performance are found to be 550–600 °C and 300–450 nm. Further studies should be focused on the preparation of micrometer thick films with the highest quality, to achieve photocurrents closer to theoretical limit.

References

(1) Kim, J. H.; Hansora, D.; Sharma, P.; Jang, J. W.; Lee, J. S. Toward Practical Solar Hydrogen Production-an Artificial Photosynthetic Leaf-to-Farm Challenge. *Chemical Society Reviews* **2019**, *48* (7), 1908–1971. https://doi.org/10.1039/c8cs00699g.

(2) Cheng, W. H.; Richter, M. H.; May, M. M.; Ohlmann, J.; Lackner, D.; Dimroth, F.; Hannappel, T.; Atwater, H. A.; Lewerenz, H. J. Monolithic Photoelectrochemical Device for Direct Water Splitting with 19% Efficiency. *ACS Energy Letters* **2018**, *3* (8), 1795–1800. https://doi.org/10.1021/acsenergylett.8b00920.

(3) Kim, J. H.; Jang, J. W.; Jo, Y. H.; Abdi, F. F.; Lee, Y. H.; Van De Krol, R.; Lee, J. S. Hetero-Type Dual Photoanodes for Unbiased Solar Water Splitting with Extended Light Harvesting. *Nature Communications* **2016**, *7*, 1–9. https://doi.org/10.1038/ncomms13380.

(4) Jia, J.; Seitz, L. C.; Benck, J. D.; Huo, Y.; Chen, Y.; Ng, J. W. D.; Bilir, T.; Harris, J. S.; Jaramillo, T. F. Solar Water Splitting by Photovoltaic-Electrolysis with a Solar-to-Hydrogen Efficiency over 30%. *Nature Communications* **2016**, *7* (May), 1–6. https://doi.org/10.1038/ncomms13237.

(5) Bozheyev, F.; Ellmer, K. Thin Film Transition Metal Dichalcogenide Photoelectrodes for Solar Hydrogen Evolution: A Review. *Journal of Materials Chemistry A* **2022**, *10*, 9327–9347. https://doi.org/10.1039/d2ta01108e.

(6) Shockley, W.; Queisser, H. J. Detailed Balance Limit of Efficiency of P-n Junction Solar Cells. *Journal of Applied Physics* **1961**, *32* (3), 510–519. https://doi.org/10.1063/1.1736034.

(7) Noureldine, D.; Takanabe, K. State-of-the-Art Sn2+-Based Ternary Oxides as Photocatalysts for Water Splitting: Electronic Structures and Optoelectronic Properties. *Catalysis Science and Technology* **2016**, *6* (21), 7656–7670. https://doi.org/10.1039/c6cy01666a.

(8) Kölbach, M.; Pereira, I. J.; Harbauer, K.; Plate, P.; Höflich, K.; Berglund, S. P.; Friedrich, D.; Van De Krol, R.; Abdi, F. F. Revealing the Performance-Limiting Factors in α-SnWO4 Photoanodes for Solar Water Splitting. *Chemistry of Materials* **2018**, *30* (22), 8322–8331. https://doi.org/10.1021/acs.chemmater.8b03883.

(9) Liu, D.; Chen, X.; Qiao, Y.; Zhou, Y.; Kuang, Y. Awakening the Photoelectrochemical Activity of A-SnWO 4 Photoanodes with Extraordinary Crystallinity Induced by Reductive Annealing . *Advanced Energy and Sustainability Research* **2022**, *3* (1), 2100146. https://doi.org/10.1002/aesr.202100146.

*Corresponding authors: farabi.bozheyev@gmail.com and mauricio.schieda@hereon.de

(10) Zhu, S.; Liu, D.; Li, J.; Kuang, Y. Chemical Vapor Deposition of Crystalized Nanoscale α-SnWO 4 Thin Films and Their Photoelectrocatalytic Properties. *ACS Applied Energy Materials* **2022**, *5*, 14372−14380. https://doi.org/10.1021/acsaem.2c02909.

(11) Ziani, A.; Harb, M.; Noureldine, D.; Takanabe, K. UV-Vis Optoelectronic Properties of α-SnWO4: A Comparative Experimental and Density Functional Theory Based Study. *APL Materials* **2015**, *3* (9), 3–8. https://doi.org/10.1063/1.4930005.

(12) Abdi, F. F.; Berglund, S. P. Recent Developments in Complex Metal Oxide Photoelectrodes. *Journal of Physics D: Applied Physics* **2017**, *50* (19), 193002. https://doi.org/10.1088/1361-6463/aa6738.

(13) Elviera; Yulizar, Y.; Apriandanu, D. O. B.; Marcony Surya, R. Fabrication of Novel SnWO4/ZnO Using Muntingia Calabura L. Leaf Extract with Enhanced Photocatalytic Methylene Blue Degradation under Visible Light Irradiation. *Ceramics International* **2022**, *48* (3), 3564–3577. https://doi.org/https://doi.org/10.1016/j.ceramint.2021.10.135.

(14) Wei, Q.; Xiong, S.; Li, W.; Jin, C.; Chen, Y.; Hou, L.; Wu, Z.; Pan, Z.; He, Q.; Wang, Y.; Tang, D. Double Z-Scheme System of α-SnWO4/UiO-66(NH2)/g-C3N4 Ternary Heterojunction with Enhanced Photocatalytic Performance for Ibuprofen Degradation and H2 Evolution. *Journal of Alloys and Compounds* **2021**, *885*, 160984. https://doi.org/https://doi.org/10.1016/j.jallcom.2021.160984.

(15) Liu, X.; Liang, B.; Li, W. In Situ Decoration of SnS Quantum Dots on the α-SnWO4 Nanosheets for Superior Visible-Light Photocatalytic Performance. *Applied Surface Science* **2020**, *531*, 147379. https://doi.org/https://doi.org/10.1016/j.apsusc.2020.147379.

(16) Azofra, L. M.; Cavallo, L.; Basset, J. M.; Harb, M. Need for Rationally Designed SnWO4Photo(Electro)Catalysts to Overcome the Performance Limitations for O2and H2Evolution Reactions. *Journal of Physical Chemistry C* **2021**, *125* (16), 8488–8496. https://doi.org/10.1021/acs.jpcc.0c11614.

(17) Bozheyev, F.; Akinoglu, E. M.; Wu, L.; Lou, S.; Giersig, M. Effect of Mo-Doping in SnO2 Thin Film Photoanodes for Water Oxidation. *International Journal of Hydrogen Energy* **2020**, *45* (58), 33448–33456. https://doi.org/10.1016/j.ijhydene.2020.09.050.

(18) Franchini, C.; Reticcioli, M.; Setvin, M.; Diebold, U. Polarons in Materials. *Nature Reviews Materials* **2021**, *6* (7), 560–586. https://doi.org/10.1038/s41578-021-00289-w.

(19) Wang, J.; Yan, H.; Long, Y.; Li, W. Enhanced Photocatalytic Property of α-SnWO4 Nanoplates by h-BN Decorating. *Journal of Materials Science: Materials in Electronics* **2021**, *32* (17), 21858–21868. https://doi.org/10.1007/s10854-021-06530-0.

(20) Liu, Y.; Qiu, W.; He, G.; Wang, K.; Wang, Y.; Chen, L.; Wu, Q.; Li, W.; Li, J. Nail-like α-SnWO4Array Film with Increased Reactive Facets for Photoelectrochemical Water Splitting. *Journal of Physical Chemistry C* **2022**, *126* (37), 15596–15605. https://doi.org/10.1021/acs.jpcc.2c04302.

(21) Schnell, P.; Dela Cruz, J. M. C. M.; Kölbach, M.; van de Krol, R.; Abdi, F. F. PH-Dependent Stability of α-SnWO4 Photoelectrodes. *Chemistry of Materials* **2022**, *34* (4), 1590–1598. https://doi.org/10.1021/acs.chemmater.1c03517.

(22) Schnell, P.; Kölbach, M.; Schleuning, M.; Obata, K.; Irani, R.; Ahmet, I. Y.; Harb, M.; Starr, D. E.; van de Krol, R.; Abdi, F. F. Interfacial Oxide Formation Limits the Photovoltage of α-SnWO4/NiOx

*Corresponding authors: farabi.bozheyev@gmail.com and mauricio.schieda@hereon.de

Photoanodes Prepared by Pulsed Laser Deposition. *Advanced Energy Materials* **2021**, *11*, 2003183. https://doi.org/10.1002/aenm.202003183.

(23) Kölbach, M.; Hempel, H.; Harbauer, K.; Schleuning, M.; Petsiuk, A.; Höflich, K.; Deinhart, V.; Friedrich, D.; Eichberger, R.; Abdi, F. F.; Van De Krol, R. Grain Boundaries Limit the Charge Carrier Transport in Pulsed Laser Deposited α-SnWO4Thin Film Photoabsorbers. *ACS Applied Energy Materials* **2020**, *3* (5), 4320–4330. https://doi.org/10.1021/acsaem.0c00028.

(24) Wang, Y.; Wang, L.; Zhang, X.; Liang, X.; Feng, Y.; Feng, W. Two-Dimensional Nanomaterials with Engineered Bandgap: Synthesis, Properties, Applications. *Nano Today* **2021**, *37*, 101059. https://doi.org/10.1016/j.nantod.2020.101059.

(25) Qiu, W.; Liu, Y. Stannous Tungstate Semiconductor for Photocatalytic Degradation and Photoelectrochemical Water Splitting: A Review. *Energies* **2022**, *15* (23), 9194. https://doi.org/10.3390/en15239194.

(26) Rettie, A. J. E.; Chemelewski, W. D.; Emin, D.; Mullins, C. B. Unravelling Small-Polaron Transport in Metal Oxide Photoelectrodes. *Journal of Physical Chemistry Letters* **2016**, *7* (3), 471–479. https://doi.org/10.1021/acs.jpclett.5b02143.

(27) He, G.; Li, W.; Qiu, W.; Xu, C.; Wang, K.; Chen, L.; Wang, Y.; Liu, Y.; Li, J. Constructing a Two-Dimensional SnWO4Nanosheet Array Film for Enhanced Photoelectrochemical Performance. *ACS Applied Energy Materials* **2022**, *5* (9), 11883–11891. https://doi.org/10.1021/acsaem.2c02547.

(28) Qiu, W.; Zhang, Y.; He, G.; Chen, L.; Wang, K.; Wang, Q.; Li, W.; Liu, Y.; Li, J. Two-Dimensional Long-Plate SnWO4Photoanode Exposed Active Facets for Enhanced Solar Water Splitting. *ACS Applied Energy Materials* **2022**, *5* (9), 11732–11739. https://doi.org/10.1021/acsaem.2c02235.

(29) Bozheyev, F.; Akinoglu, E. M.; Wu, L.; Lu, H.; Nemkayeva, R.; Xue, Y.; Jin, M.; Giersig, M. Band Gap Optimization of Tin Tungstate Thin Films for Solar Water Oxidation. *International Journal of Hydrogen Energy* **2020**, *45* (15), 8676–8685. https://doi.org/10.1016/j.ijhydene.2020.01.126.

(30) Bozheyev, F.; Fengler, S.; Kollmann, J.; Klassen, T.; Schieda, M. Transient Surface Photovoltage Spectroscopy of (NH4)2Mo3S13/WSe2 Thin-Film Photocathodes for Photoelectrochemical Hydrogen Evolution. *ACS Applied Materials & Interfaces* **2022**, *14*, 22071–22081. https://doi.org/10.1021/acsami.2c01623.

(31) Akl, A. A.; Kamal, H.; Abdel-Hady, K. Characterization of Tungsten Oxide Films of Different Crystallinity Prepared by RF Sputtering. *Physica B: Condensed Matter* **2003**, *325*, 65–75. https://doi.org/10.1016/S0921-4526(02)01431-X.

(32) Abduvalov, A.; Kaikanov, M.; Atabaev, T. S.; Tikhonov, A. Improving Photoelectrochemical Activity of Magnetron-Sputtered Double-Layer Tungsten Trioxide Photoanodes by Irradiation with Intense Pulsed Ion Beams. *Nanomaterials* **2022**, *12* (15), 2639. https://doi.org/10.3390/nano12152639.

(33) Solis, J.; Frantti, J.; Lantto, V.; Häggström, L.; Wikner, M. Characterization of Phase Structures in Semiconducting Powders by Mössbauer and Raman Spectroscopies. *Physical Review B - Condensed Matter and Materials Physics* **1998**, *57* (21), 13491–13500. https://doi.org/10.1103/PhysRevB.57.13491.

(34) Jariwala, D.; Davoyan, A. R.; Wong, J.; Atwater, H. A. Van Der Waals Materials for Atomically-Thin Photovoltaics: Promise and Outlook. *ACS Photonics* **2017**, *4* (12), 2962–2970.

*Corresponding authors: farabi.bozheyev@gmail.com and mauricio.schieda@hereon.de

https://doi.org/10.1021/acsphotonics.7b01103.

(35) Bozheyev, F.; Akinoglu, E. M.; Wu, L.; Lu, H.; Nemkayeva, R.; Xue, Y.; Jin, M.; Giersig, M. Band Gap Optimization of Tin Tungstate Thin Films for Solar Water Oxidation. *International Journal of Hydrogen Energy* **2020**, *45*, 8676–8685. https://doi.org/10.1016/j.ijhydene.2020.01.126.

(36) Hutchins, M. G.; Abu-Alkhair, O.; El-Nahass, M. M.; El-Hady, K. A. Structural and Optical Characterisation of Thermally Evaporated Tungsten Trioxide (WO3) Thin Films. *Materials Chemistry and Physics* **2006**, *98* (2–3), 401–405. https://doi.org/10.1016/j.matchemphys.2005.09.052.

(37) Thomas, D.; Mainz, R.; Rodriguez-Alvarez, H.; Marsen, B.; Abou-Ras, D.; Klaus, M.; Genzel, C.; Schock, H. W. In-Situ Studies of the Recrystallization Process of CuInS2 Thin Films by Energy Dispersive X-Ray Diffraction. *Thin Solid Films* **2011**, *519* (21), 7193–7196. https://doi.org/10.1016/j.tsf.2010.12.229.

(38) Nakajima, H. The Discovery and Acceptance of the Kirkendall Effect: The Result of a Short Research Career. *JOM* **1997**, *49* (6), 15–19. https://doi.org/10.1007/BF02914706.

(39) Xiao, Y.; Chen, X.; Jiang, Q.; Feng, C. Synthesis of SnW3O9/C as Novel Anode Material for Lithium-Ion Battery Application. *Journal of Materials Science: Materials in Electronics* **2021**, *32* (19), 23935–23943. https://doi.org/10.1007/s10854-021-06853-y.

(40) Zhu, G.; Que, W.; Zhang, J.; Zhong, P. Photocatalytic Activity of SnWO4 and SnW3O 9 Nanostructures Prepared by a Surfactant-Assisted Hydrothermal Process. *Materials Science and Engineering B: Solid-State Materials for Advanced Technology* **2011**, *176* (18), 1448–1455. https://doi.org/10.1016/j.mseb.2011.08.003.

(41) He, G.; Li, J.; Qiu, W.; Chen, L.; Wang, K.; Liu, Y.; Liu, M.; Li, W. Engineering Surficial Atom Arrangement on α-SnWO4 Film for Efficient Photoelectrochemical Water Splitting. *Chemical Engineering Journal* **2023**, *469* (May), 144096. https://doi.org/10.1016/j.cej.2023.144096.

(42) Kong, H.; Abdi, F. F. Recent Progress in the Development of Tin Tungstate (α-SnWO 4) Photoanodes for Solar Water Oxidation. *Inorganic Chemistry Frontiers* **2023**, *10*, 7109–7125. https://doi.org/10.1039/d3qi01841e.

Acknowledgements

F.B. gratefully acknowledges funding by the Alexander-von-Humboldt Foundation through Georg Forster Research Fellowship, Germany. This research has been funded by the Science Committee of the Ministry of Science and Higher Education of the Republic of Kazakhstan: Grant No. AP19679991 and BR21882187. Special thanks to Sebastian Weitz for the preparation of the cross-section specimens for the SEM-EDX analyses in Helmholtz Zentrum Berlin, Germany.

Supporting Information available. Additional experimental details, photographs of experimental setup, optical images of the films, ellipsometry, XRD, Raman spectra of all compounds, and PEC measurements.

*Corresponding authors: farabi.bozheyev@gmail.com and mauricio.schieda@hereon.de

Table Of Contents

